Wingsail performance in unsteady atmospheric surface layer winds

Clément Bouhourd, Laurent Perret, Carlo Cossu

Ocean Engineering 314 (2024) 119653

Contents lists available at ScienceDirect

Ocean Engineering

journal homepage: www.elsevier.com/locate/oceaneng

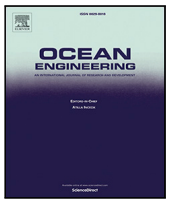

Research paper

Wingsail performance in unsteady atmospheric surface layer winds

Clément Bouhourd, Laurent Perret, Carlo Cossu *

Hydrodynamics, Energetics and Atmospheric Environment Research Laboratory (LHEEA), CNRS - École Centrale de Nantes - Nantes Université, 1 rue de la Noë, Nantes F-44300, France

ARTICLE INFO

Keywords:
Wind-assisted ship propulsion (WASP)
Unsteady aerodynamics
Atmospheric surface layer
Turbulence

ABSTRACT

The performance of wind propulsion systems is evaluated in unsteady inhomogeneous winds with tools that are routinely used to predict the performance of wind turbines and which give access to the unsteady aerodynamic forces acting on the wingsail. A rigid wingsail exposed to a realistic atmospheric surface layer wind is used as a testbed. For this case, we show that standard deviations of the aerodynamic driving force are larger than 15%–20% of the mean values when the true wind velocity is larger than the ship speed. We also show that the mean aerodynamic driving forces computed by averaging the unsteady driving forces are only slightly smaller than the ones computed on the mean wind despite the strongly nonlinear dependence of the unsteady forces on the wind velocity and direction.

1. Introduction

The current high and volatile oil prices as well as the increasingly demanding regulations on greenhouse gas emissions are driving a renewed interest in wind-assisted propulsion for shipping as a tool to increase the efficiency and the sustainability of maritime trade (Laursen et al., 2023). While sailing is as old as civilization, the prediction and the optimization of the performance of wind propellers such as kites, Flettner rotors, suction sails and wingsails is still a matter of interest and active research. In the following we consider wingsails as a testbed for our analysis of the effects of unsteady winds and atmospheric turbulence on the aerodynamic performance of these systems.

Wingsails have been introduced more than half a century ago mainly in the context of racing multihulls, such as C–Class catamarans (see e.g. Marchaj, 1996; Turnock et al., 2014) evolving into the sophisticated systems installed e.g. on 2017 America's cup AC50 foiling catamarans whose speed U_S is typically larger than the mean true wind speed U_T with mean velocity ratios $\eta = U_S/U_T$ attaining values of $\approx$1.5 to 2.5. In this operating regime the apparent wind seen onboard is mainly composed of the boat speed with a substantial dilution of turbulence intensity and vertical shear of the true (atmospheric) wind. For these applications, therefore, it made sense to use methods developed for aeronautical applications where $\eta \gg 1$ and the incoming flow is typically assumed uniform with very low levels of freestream turbulence (see e.g. Fossati, 2009). However, in situations where wingsails are used as auxiliary propulsion systems on commercial vessels, most of the cumulated wind-induced propulsive power is produced when the mean true wind is comparable or larger than the (usually only moderate) ship speed, i.e. in situations where $\eta \lesssim 1$ to 1.5. In this regime the unsteadiness and the vertical gradient of the true wind do strongly affect the apparent wind. Furthermore, additional shear and unsteadiness may result from the interaction of the incoming wind with the ship hull and the superstructures and many questions arise about the influence of these effects on wingsails performance: What is the influence of wind unsteadiness on the mean aerodynamic forces? How precise are the estimation of these forces based on mean-wind profiles? How large are the fluctuations of aerodynamic forces? How do these unsteady effects combine with those of the apparent wind veering associated to true wind vertical gradients?

In this study we address the questions raised above by computing the unsteady aerodynamic forces exerted on a model wingsail exposed to the turbulent wind of the neutral atmospheric surface layer. The unsteady forces acting on the wingsail are computed by using methods that are now standard in the analysis and design of wind turbines and that give access to the unsteady aerodynamic forces. Particular attention will be given to the comparison of these unsteady forces and their mean value computed with a fully unsteady formulation to those computed in the quasi-steady approximation and those based on only the mean value of the wind.

The paper is organized as follows. The problem is set in Section 2, by defining the wingsail properties and the models used to compute the aerodynamic forces acting on it, with details of numerical methods detailed in Appendix. A preliminary analysis is developed in Section 3 by computing the performance of the wingsail exposed to an idealized uniform wind with periodic fluctuations. The more realistic turbulent

* Corresponding author.
E-mail addresses: Clement.Bouhourd@EC-Nantes.fr (C. Bouhourd), Laurent.Perret@EC-Nantes.fr (L. Perret), Carlo.Cossu@CNRS.fr (C. Cossu).

https://doi.org/10.1016/j.oceaneng.2024.119653
Received 4 July 2024; Received in revised form 9 October 2024; Accepted 27 October 2024

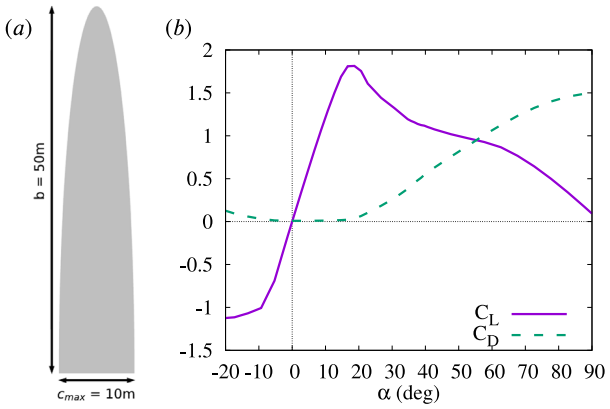

Fig. 1. (*a*) Wingsail planview and (*b*) lift and drag coefficients C_L, C_D of the FFA-W3-241 airfoil versus the angle of attack.

true winds of a thermally-neutral atmospheric surface layer are computed by large-eddy simulations and the wingsail performance then analyzed as a function of true wind angle and the ship-to-wind speed ratio in Section 4. The main results and their implications are discussed in Section 5.

2. Problem setting

Wingsail model. We consider an idealized wingsail, shown in Fig. 1*a*, of half-elliptic shape 50 m tall (major half-axis) with 10 m maximum chord near the ground (minor axis). FFA-W3-241 wing profiles are used as longitudinal airfoil sections, with their lift and drag coefficients available in standard numerical codes used for the simulation of the reference DTU 10-MW wind turbine (Bak et al., 2013; Fuglsang et al., 1998). The lift and drag coefficients dependence on the angle of attack α for the chosen airfoil are reported in Fig. 1 with α measured from the angle of zero lift. The effect of lift-enhancing devices such as flaps or suction slots is not considered but it is assumed that the wingsail can be twisted to adapt to the mean apparent wind veer, when deemed appropriate.

Evaluation of aerodynamic forces. The main goal of this study is to compute the performance of wingsails by using unsteady and inhomogeneous wind data. Standard methods based on vortex lines are not well adapted to the unsteady case because not only the lift and the drag produced by every wing section depend on time, but also the vorticity shed in the wake, its turbulent diffusion and the wake geometry itself. To take into due account these effects we have resorted to a blade-element approach where aerodynamic forces are computed dividing the wingsail in a finite number of elements along the spanwise direction and then computing the aerodynamic forces on each section which is exposed to the local value of the wind combined to the wake-induced velocity. The local aerodynamic force acting on each wingsail element is computed by means of both the quasi-steady formulation and an adapted Beddoes–Leishman model (Leishman and Beddoes, 1989; Leishman, 2006; Damiani and Hayman, 2019) of the unsteady lift and drag generation. In the quasi-steady approach aerodynamic forces are computed by using the steady tabulated data of $C_L(\alpha), C_D(\alpha)$ assuming that the generation of the aerodynamic force (lift and drag) is instantaneous. In the fully unsteady formulation the Beddoes–Leishman model is used to take into account the temporal delays between angle of attack changes and force generation in both the attached and the stalled regimes.[1] Temporal and spanwise variations of the aerodynamic force generate vorticity which is shed into and then advected by the vortical wake. We have resorted to the convected Lagrangian elements method to model the unsteady free vortex wake (Shaler et al., 2020, 2023) and the associated unsteady induced velocity on the wingsail. All these methods were implemented in the code that we have used in this study, which is the state of the art tool in the wind energy community for the simulation of wind turbines exposed to turbulent incoming winds. We refer the reader to Appendix for more details on the methods.

The effect of the ground is enforced by the method of mirror images in the computation of the wake-induced velocity components. To prevent a dependence of the results on the details of the ground modeling and distance from the wingsail base, we assume that there is no space between the wing base and the ground (this assumption can be easily removed in future more detailed studies of more specific configurations).

Examples of the computed wakes developing downstream of the wingsail are shown in Fig. 2 for the cases of a uniform wind (panel *a*) and of two types of unsteady winds (panels *b* and *c*). In all cases, the usual tip vortex begins to form from the curling wake downwind to the wingsail top. However, while the wake develops along quasi-straight lines in the streamwise direction when advected by a uniform wind, this is no more true in unsteady winds.

3. Wingsail performance in a time-periodic unsteady wind

It is instructive to consider, as a first case, a uniform wind subjected to a periodic perturbation:

$$u(t) = U\,[1 + A\cos(\omega t)]\,; \quad v(t) = U\,A\sin(\omega t), \tag{1}$$

where the circular frequency ω can be expressed in terms of the (dimensionless) reduced frequency k as $\omega = 2kU/c_{max}$. The unsteady aerodynamic forces are computed on the half-elliptic wingsail trimmed to the $\alpha_{wing} = 20°$ angle (with respect to the mean wind direction) which maximizes the lift computed with the (temporally-averaged) mean wind (black solid line in Fig. 3). Computations are performed for the reduced frequencies $k = 0.01$, $k = 0.1$ and $k = 0.5$ with a mean velocity $U = 10$ m/s and a perturbation amplitude A=7% inducing velocity magnitudes changing by ±7% and angles of attack $\alpha = \alpha_{wing} - \alpha_{wind}$ ranging from 16° to 24°.

The unsteady time-periodic lift responses $L(t)$ to the periodic oscillations of the incoming wind are reported in Fig. 3 versus the instantaneous angle of attack $\alpha(t)$. When the quasi-steady model is used (panel *a* in the figure), the unsteady lift responses corresponding to all the considered reduced frequencies k almost collapse on the same limit cycle, with residual differences due to unsteady wake effects. The hysteresis in the lift cycle can be attributed to quarter-period phase lags between the wind velocity magnitude $|\mathbf{u}| = U[1 + A^2 + 2A\cos(\omega t)]^{1/2}$ and the wind angle $\alpha_{wind} = \tan^{-1}(v/u)$. When the wind angle is zero ($\omega t = n\pi$) and $\alpha = 20°$, the velocity magnitude $|\mathbf{u}|$ can be at its minimum or maximum value $u = U(1 \pm A)$, depending on the phase in the cycle (even or odd value of the integer n) inducing a lower or higher dynamic pressure and therefore a lower or higher lift, as indeed observed.

When the Beddoes–Leishman model is used instead of the quasi-steady model (see panel *b* of Fig. 3), a differentiation of the lift cycles corresponding to different values of k appears. For the low reduced frequency $k = 0.01$, as expected, the response is similar to the one obtained with the quasi-steady approach but this is no longer the case for the larger values $k = 0.1$ and $k = 0.5$ where lift generation time-delays effects on the periodic lift response cycles are increasingly important.

[1] As the wing is not a bluff-body with a well-defined shedding frequency for coherent quasi-2D structures, and is fixed, nonlinear models of the aerodynamic force used in the wind-engineering vortex-induced-vibrations (see e.g. Blevins, 1990; Chen et al., 2020) are not applicable to the presently considered case.

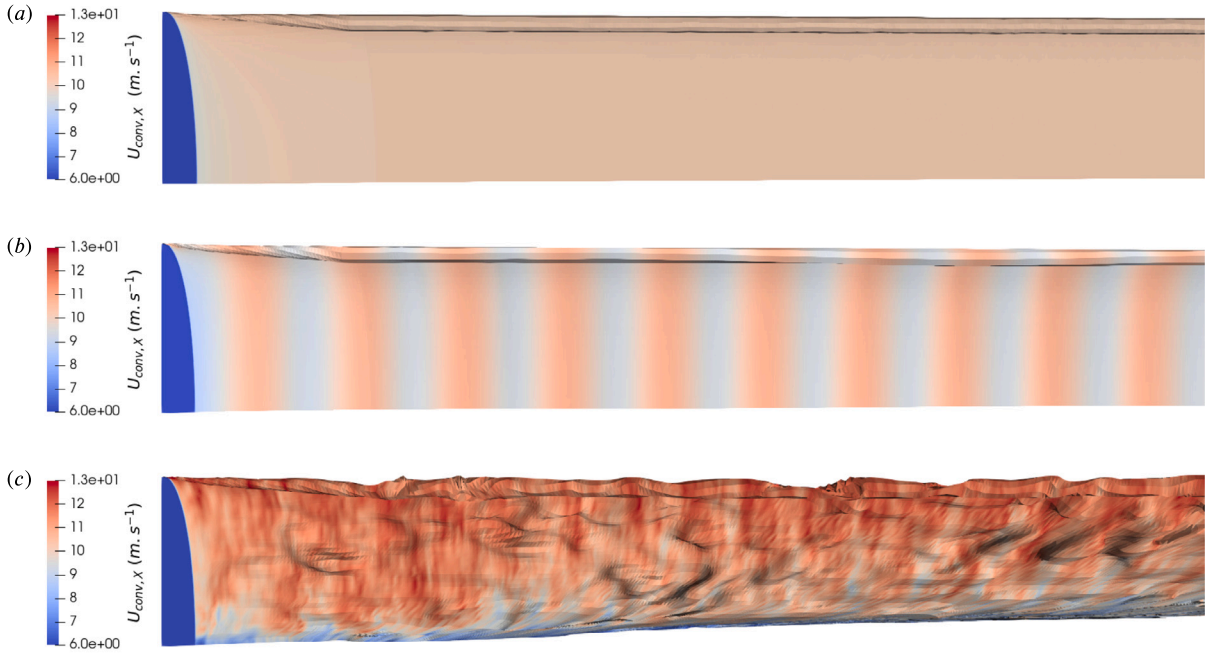

Fig. 2. Examples of wakes developing downstream of the wingsail exposed to (*a*) a uniform wind, (*b*) a uniform wind with time-periodic perturbations (*c*) an atmospheric surface-layer wind. The color-scale indicates the local wake advection velocity.

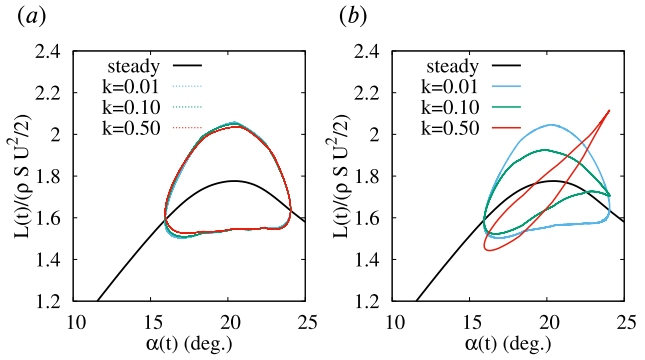

Fig. 3. Effects of periodic wind fluctuations on the instantaneous lift for computations based on the quasi-steady formulation (panel (*a*), dashed lines) and the Beddoes–Leishman model (panel (*b*), solid lines). The lift periodic response is computed for three values of the reduced frequency k and compared to the steady response computed in the absence of periodic perturbations (black solid line). The instantaneous lift $L(t)$ is normalized with respect to mean dynamic pressure $\rho SU^2/2$, where U is the mean wind velocity, and are reported versus the instantaneous angle of attack $\alpha(t)$.

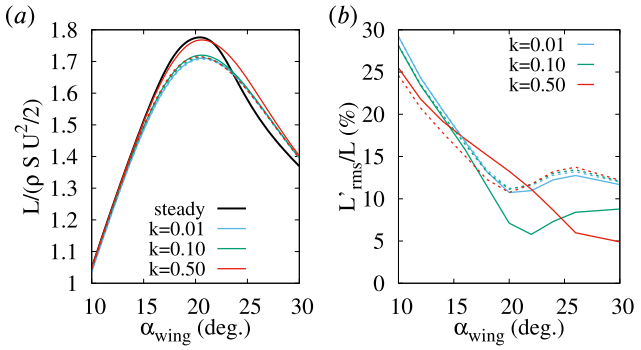

Fig. 4. Effects of periodic wind fluctuations on (a) the wingsail mean lift normalized with the mean dynamic pressure $\rho SU^2/2$ and, (b) the lift relative standard deviation L'_{rms}/L. Results computed for the three selected reduced frequencies with the Beddoes–Leishman model (solid colored lines) are compared to those obtained with the quasi-steady formulation (colored dashed lines). The mean lift is also compared to the one computed with the (steady) mean wind (solid black line in panel *a*).

One important question is to understand how the unsteady wind fluctuations affect the time-averaged aerodynamic force and its standard deviation. To this end, the mean (time-averaged) lift and its relative standard deviation (the root-mean-squared lift fluctuations divided by the mean lift L'_{rms}/L) have been computed for a range of wing trim angles α_{wing}, as shown in Fig. 4. From panel (*a*) of this figure it can be seen that, for the considered periodic specific wind fluctuations, the temporally-averaged (unsteady) lift is similar to the one computed using the mean wind profile; it is almost identical for small angles of attack (far from stall) and slightly larger far beyond stall. All the values computed with the quasi-steady approach almost coincide and are smaller than the one computed with the mean wind near the lift peak value of the trim angle. The mean lift values computed with the Beddoes–Leishman model are similar to those computed with the quasi-steady approach, except for the highest considered reduced frequency $k = 0.5$ for which they almost coincide with those computed using the mean wind up the mean lift peak.

The unsteady computations give also, most importantly, access to the temporal fluctuations of the aerodynamic forces which are not accessible when using the mean wind profile. The root-mean-squared *rms* (standard deviation) value of the lift fluctuations is reported in Fig. 4*b* in terms of percentage of the mean lift. The two considered models (QS and BL) predict a similar trend for the relative fluctuations in the attached flow regime ($\alpha_{wing} \lesssim 15°$) for all the considered values of k. Fluctuations computed with the quasi-steady approach remain insensitive to k even for higher trim angles in the stalled regime with a relative minimum value of L'_{rms}/L obtained near the angle maximizing the mean lift. At this mean lift peak value of the trim angle, however, the relative fluctuation level computed with the Beddoes–Leishman model, depends non-monotonically on the reduced frequency k varying from $\approx 6\%$ for $k = 0.1$ to $\approx 15\%$ for $k = 0.5$.

This first analysis of the influence of wind unsteadiness and of the model used for the computation of the forces on the wingsail performance has been obtained on a very idealized case of time-periodic wind oscillations with a specific phase lag between wind magnitude

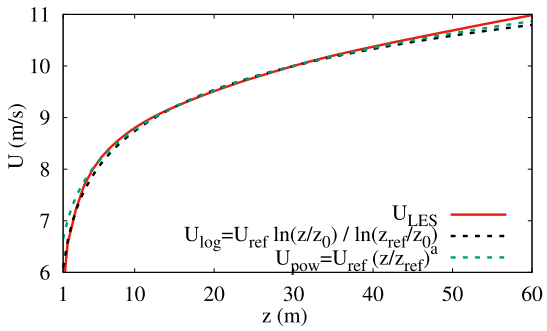

Fig. 5. Comparison of the mean velocity profile $U_{LES}(z)$ computed by large-eddy simulations with the theoretical logarithmic profile $U_{\log}$ and the power law fit U_{pow} with $z_{ref} = 30$ m, $U_{ref} = 10$ m/s, $z_0 = 0.005$ m, $a = 0.12$.

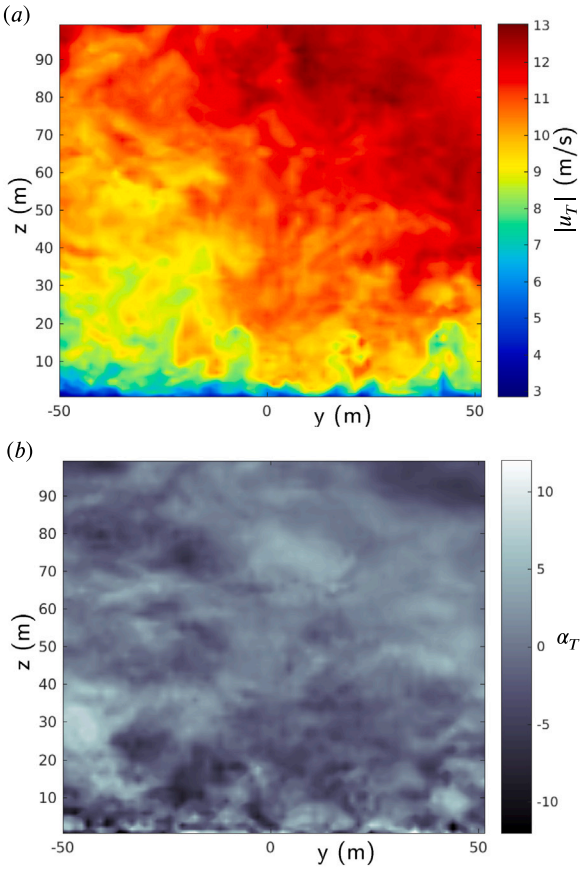

Fig. 6. Snapshot of (a) the true wind horizontal velocity magnitude and (b) horizontal direction angle α_T in the y–z cross-stream plane orthogonal to the mean true wind direction of the simulated atmospheric surface layer computed by dedicated large-eddy simulations. Wind magnitudes are expressed in m/s, y and z coordinates in meters and angles in degrees. Note that the considered wingsail extends up to $z = 50$ m height.

and wind direction oscillations and with spatially-uniform mean winds and perturbations. In the next section we consider the more realistic case of a moving wingsail immersed in the atmospheric surface-layer turbulent wind, where the wind is spatially inhomogeneous and its temporal spectrum is broadband.

4. Wingsail performance in atmospheric surface layer winds

The true wind. The main objective of this study is to compute the wingsail performance in realistic winds of the atmospheric boundary

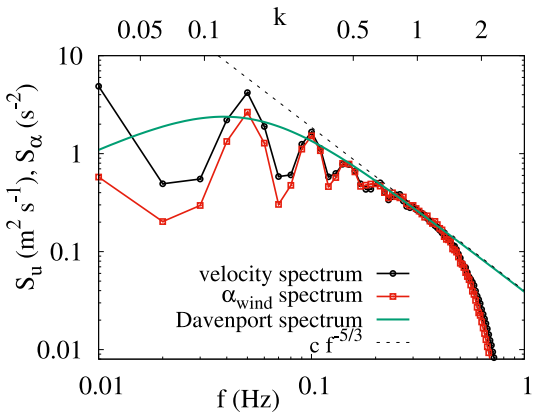

Fig. 7. Power spectral density of the true wind velocity (black line with circular symbols) and of the true wind angle (red line with square symbols) at $z = 30$ m. The Davenport spectrum and the Kolmogorov inertial spectrum dependence $f^{-5/3}$ are also reported for comparison. All spectra are normalized so as to have the same amplitude as the velocity spectrum in the inertial range. Data are expressed both in terms of the dimensional frequency (bottom horizontal axis) and of the (dimensionless) reduced frequency $k = \pi f c / U_T$ (top horizontal axis).

layer (ABL). Currently installed and planned wingsails do not exceed ≈100 m in height and are therefore confined to the lowest part of the ABL, the atmospheric surface layer (ASL) where Coriolis acceleration effects can be neglected and Monin–Obhukov similarity theory applies (Monin and Obukhov, 1954; Wyngaard, 2010). In the analysis we will consider a neutral atmosphere, where the air has the same (constant, homogeneous) temperature as the sea, for which the theory predicts the logarithmic dependence on height of the true wind mean velocity $U_{log} = (u_*/\kappa)\log(z/z_0)$ where u_* is the friction velocity, κ the Von Karman constant and z_0 the ground roughness length scale. For practical purposes, the mean velocity at the reference height is used to evaluate u_* giving $U_{log}(z) = U_T(z_{ref})\log(z/z_0)/\log(z_{ref}/z_0)$.

The unsteady wind is computed with a numerical code specifically designed to simulate atmospheric boundary layers by means of large-eddy simulations (see Appendix for details). The pressure gradient maintaining the wind in the numerical simulation is dynamically adjusted so as to enforce a constant $U_T = 10$ m/s mean (averaged in the x-y horizontal plane) true wind at $z_{ref} = 30$ m height (the T subscript indicates the true wind which is measured in a non-moving frame). The roughness length $z_0 = 0.005$ m is chosen in the 10^{-4} m – 10^{-2} m range of those typical of open seas conditions (see e.g. DNV-GL, 2019). The computed mean wind profile $U_T(z)$ is close to the theoretical logarithmic profile and is also well fitted by the power law $U_{pow}(z) = U_T(z_{ref})(z/z_{ref})^a$ with the value $a = 0.12$ typical of open seas conditions (see e.g. DNV-GL, 2019), as shown in Fig. 5, despite the relatively short averaging times used in this study (10^3 s i.e. ≈ 16 minutes). The streamwise turbulence intensity $I_u = \sigma_u/U_T$ (where σ_u is the standard deviation of the streamwise velocity) of the considered true wind varies from slightly more than 17% near the ground to slightly less than 10% at $z = 50$ m. Turbulent fluctuations result in a highly fluctuating and inhomogeneous wind velocity field, as shown in Fig. 6 by the snapshots of the horizontal wind magnitude and direction in a cross-plane (y-z) orthogonal to the (x-axis) mean true wind direction. The power spectral density of this unsteady wind measured at the reference height of 30 m, shown in Fig. 7, displays the expected $f^{-5/3}$ slope in the inertial range and is reasonably well fitted by Davenport's model spectrum which is well adapted to 10 min temporal averages (e.g. DNV-GL, 2019). The most energetic part of the spectrum resides in low frequencies $f \lesssim 0.2$ Hz, corresponding to reduced frequencies $k \lesssim 0.5$. Wingsail performance will be computed in this unsteady and inhomogeneous wind field.

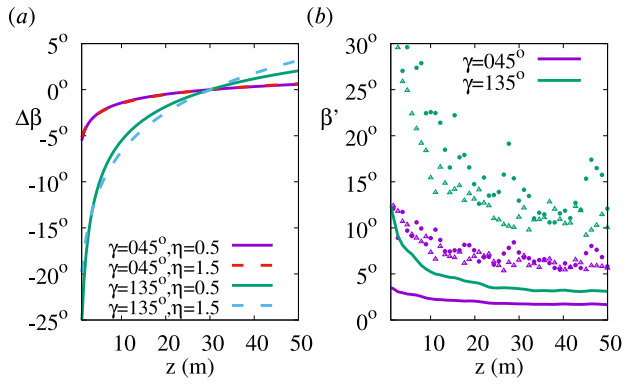

Fig. 8. (*a*) Deviation $\Delta\beta(z) = \beta(z) - \beta(z_{ref})$ of the mean apparent wind angle β from the angle at $z_{ref} = 30$ m versus height z for the two selected true wind angles $\gamma = 45°$ and 135° and the two selected velocity ratios $\eta = 0.5$ and $\eta = 1.5$. (*b*) Unsteady fluctuations β' of the apparent wind angle versus height z for the velocity ratio $\eta = 0.5$ and the two selected true wind angles. Standard deviations of β' are reported with lines while filled and empty symbols respectively denote the absolute value of the maximum positive and negative values of β'. Angles are expressed in degrees and the heights in meters.

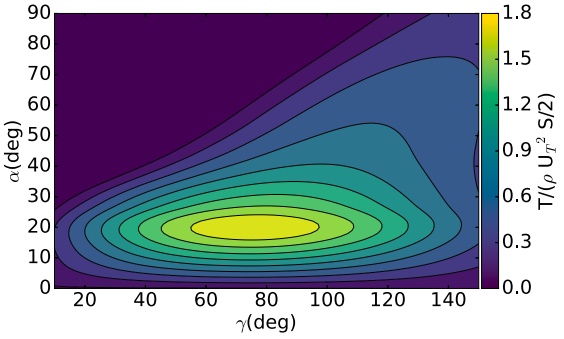

Fig. 9. Dependence of the aerodynamic driving force (thrust) coefficient, based on the reference mean true wind velocity, on the true wind angle (horizontal axis) and the wingsail trim angle (vertical axis) both expressed in degrees. The force is computed using the mean wind profiles for $\eta = 0.5$.

Apparent wind. On a ship making course at constant speed $\mathbf{U}_S$ and exposed to the true wind $\mathbf{u}_T$, the apparent wind measured onboard is $\mathbf{u}_A = \mathbf{u}_T - \mathbf{U}_S$. We denote by $\mathbf{U}_T(z)$ and $\mathbf{U}_A(z)$ the mean true and apparent wind, respectively. The angles formed by $\mathbf{U}_A$ and $\mathbf{U}_T$ (both measured at the reference height z_{ref}) with the ship velocity vector are respectively denoted by β (apparent-wind angle, AWA) and γ (true-wind angle, TWA). The presence of vertical shear in the $\mathbf{U}_T(z)$ profile results in the well-known vertical variation $\Delta\beta(z)$ of the mean apparent wind angle (wind veer) which depends on γ and the ship-to-wind velocity ratio $\eta = U_S/U_T(z_{ref})$, with a dependence more pronounced on the former, as shown in Fig. 8*a*. The inhomogeneity and unsteadiness of $\mathbf{u}_T$ result in fluctuations $\mathbf{u}' = \mathbf{u}_T - \mathbf{U}_T = \mathbf{u}_A - \mathbf{U}_A$ of the true and the apparent wind resulting in fluctuations of the wind direction. An example of the vertical dependence of the fluctuations β' of the apparent wind direction is shown in Fig. 8*b* for the velocity ratio $\eta = 0.5$. This figure shows that, for the same true wind, the fluctuations of the apparent wind direction are more pronounced when the ship runs aways from the wind (the $\gamma = 135°$ case) than when it moves towards the wind (case with $\gamma = 45°$) and that they decrease with height.

Thrust evaluation in the mean wind. We analyze the wingsail performance by computing the aerodynamic driving force i.e. the projection of the aerodynamic force on the direction of the ship velocity, which depends on the wingsail trim angle, which defines the angle of attack on the wing, but also on the wind direction with respect to the ship axis. In the following, for the sake of brevity, we will often refer to the aerodynamic driving force, as aerodynamic thrust force, or simply "thrust" and will denote it by T.

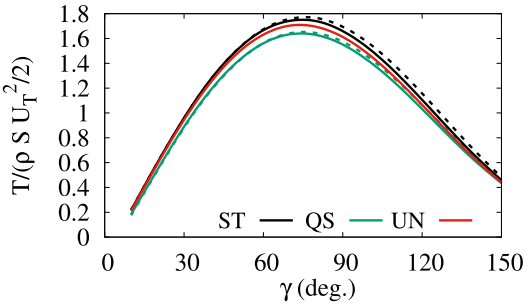

Fig. 10. Dependence of the mean thrust coefficient on the true wind angle γ for $\eta = 0.5$ for the untwisted (solid lines) and the optimally twisted (dashed lines) wingsails. Data have been computed using the mean wind (ST case, black lines) and using the unsteady wind with the quasi-steady (QS case, green lines) and the Beddoes–Leishman fully unsteady (UN case, red lines) aerodynamic models respectively.

It is instructive to initially follow the current standard approach of using the (steady) mean true wind $\mathbf{U}_T$ to compute the apparent wind and the mean thrust T. We will refer to this approach as the "steady" approach (ST). Two wings configurations will be considered: (a) an optimally twisted wing whose twist exactly compensates the apparent wind veer $\alpha_{twist}(z) = \Delta\beta(z)$ for the considered mean apparent wind which depends on γ and η and (b) a planar (untwisted) wing. We initially consider a "windy" situation in which the reference true wind speed is twice the ship speed ($\eta = 1/2$) and consider a set of true-wind angles γ ranging from 10° to 150° and a set of wingsail trim angles α_{wing} ranging from zero to 90°, where α_{wing} is the angle of attack of the wingsail section at z_{ref} with respect to the mean apparent wind $\mathbf{U}_A(z_{ref})$ at the same height. In Fig. 9 the normalized thrust $T/(\rho U_{T,ref}^2 S/2)$, is reported versus γ and α_{wing} for an optimally twisted wing, to avoid a strong dependence of the results on the apparent wind vertical veer. From this figure it can be seen that for true wind angles $30° \lesssim \gamma \lesssim 140°$ where significant levels of thrust are produced, the maximum thrust is obtained trimming the wingsail to $\alpha_{wing}^{opt} \approx 20°$, a value almost independent of γ, with aerodynamic forces mainly composed of lift. This value is slightly larger than the optimal angle of attack of the 2D wing profile because, for the finite 3D wing, the enforced angle of attack must compensate for the induced drag that reduces the effective angle of attack. Similar results are found for the untwisted wingsail (not shown).

Effect of unsteadiness on the thrust. To evaluate the effect of unsteadiness on the thrust, we have recomputed it by exposing the wingsail to the (non-averaged, unsteady) apparent wind $\mathbf{u}_A$ corresponding to the velocity ratio $\eta = 0.5$ for the selected set of true-wind angles γ. The wingsail is trimmed to the optimal value α_{wing}^{opt} computed on the mean flow at the same γ. For each considered value of γ, the thrust forces are then averaged in time and over a set of spanwise locations of the mast (every 10 m in the following) covering the whole spanwise extent (200 m) of the available true wind data to obtain the mean thrust averaged in time and space. As in Section 3 two types of computation have been performed for each case: the first using the quasi-steady approach (QS) and the second with the fully unsteady approach (UN) based on the Beddoes–Leishman model. In Fig. 10 the mean thrusts computed with the fully unsteady (UN) and quasi-steady (QS) models are compared with that obtained using the mean wind (ST model) for both the optimally twisted (solid lines) and untwisted (dashed lines) wingsails. All curves, traced versus the true mean wind angle, follow a similar trend, with the maximum thrust attained for $\gamma \approx 75°$. The maximum thrust computed with the mean flow profile, however, is overestimated by ≈ 7% with respect to the quasi-steady approach results and ≈3% with respect to the fully unsteady approach

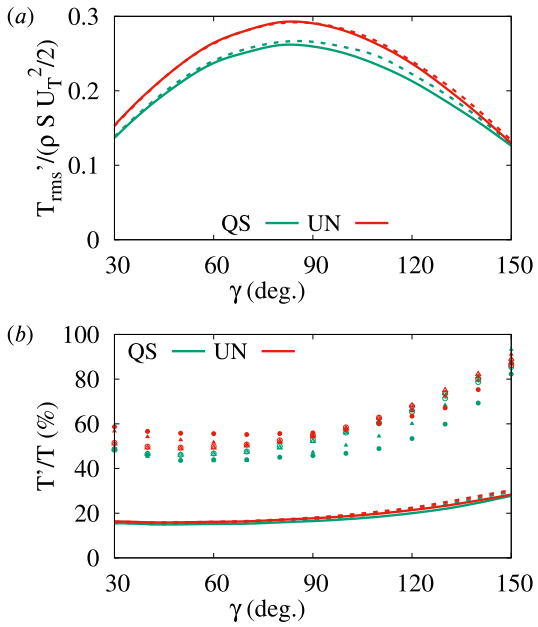

Fig. 11. Thrust fluctuations versus the true wind angle γ for $\eta = 0.5$ for the untwisted (solid lines) and the optimally twisted (dashed lines) wingsails computed using the unsteady wind and the quasi-steady (QS case, green lines) and the fully unsteady (UN case, red lines) aerodynamic model respectively. (*a*) *rms* fluctuation coefficient based on the reference mean true wind velocity, (*b*) relative fluctuations (expressed in percentage) with respect to the mean thrust with *rms* reported as solid lines and the maximum positive and negative fluctuations reported as filled and empty symbols respectively.

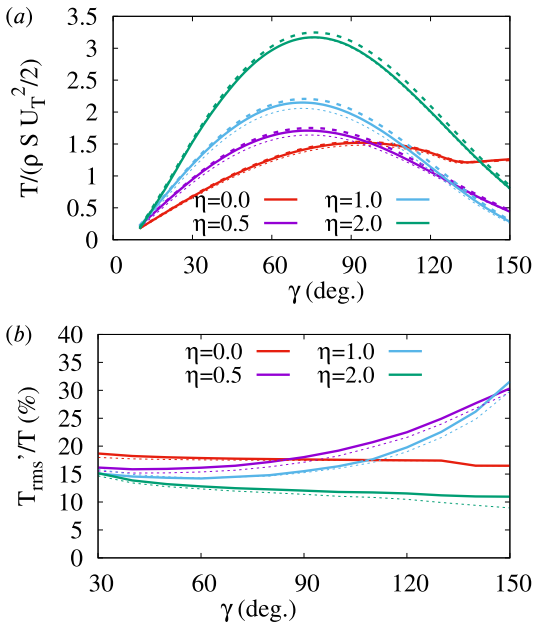

Fig. 12. Thrust dependence on the true wind angle γ for a selected set of velocity ratios η for the untwisted wingsail. (*a*) Mean thrust coefficients are based on the reference mean true wind speed. Data computed using the fully unsteady aerodynamic model are reported with solid lines, those computed with the quasi-steady model as thin dotted lines while those based on steady computations using the mean wind are reported with thick dashed lines. (*b*) Standard deviation of thrust fluctuations relative to the mean thrust at the same γ (expressed in percentage values).

results. Differences between the results obtained on the untwisted (the solid lines in the figure) and optimally twisted (dashed lines) wingsails are almost negligible. The most relevant results of the fully unsteady computations, however, concern thrust fluctuations, which are not accessible in analyses based on the mean wind. The absolute and relative values of those fluctuations are reported in Fig. 11, where their standard deviation (*rms* value) as well as the maximum values of positive and negative relative deviations are shown. Fluctuations *rms*-amplitudes are always larger than $\approx 20\%$ of the mean value, in particular when the true wind angle is increased above $\approx 90°$. The fluctuations levels computed with the fully unsteady approach are larger than those computed with the quasi-steady approach. Maximum fluctuation deviations from the mean are 2.5 to 3 times larger than their standard deviation, and always above $45-50\%$ of the mean value. Finally, we find that, for the considered case, optimally twisting the wingsail results in almost negligible improvements of the mean thrust and of its standard deviation when compared to a planar untwisted configuration.

Influence of the velocity ratio η on unsteady effects. To understand the effect of the ship to wind velocity ratio η on the previously discussed results, the thrust computations have been repeated for the additional values $\eta = 0$ (the limit where the ship velocity is negligible with respect to the true mean wind speed), $\eta = 1$, and $\eta = 2$ (the ship travels faster than the true mean wind). The mean and fluctuating thrust results are reported in Fig. 12*a* and Fig. 12*b* respectively. The general trend of all thrust curves is the expected one, with maximum thrust increasing with η because of the increase of the apparent wind velocity for the optimal γ values. Concerning thrust fluctuations, their *rms* values remain below 20% and 15% of the mean thrust for $\eta = 0$ and $\eta = 2$ respectively while they grow above these values for the intermediate η values 0.5 and 1, when $\gamma \gtrsim 90°$ where the apparent wind mean velocity, and therefore the mean thrust, become small.

From Fig. 12 it can also be seen that (a) the mean thrust and the *rms* thrust fluctuations issued from the quasi-steady and the fully unsteady computations give almost identical results for $\eta = 2$ with very slight differences appearing for smaller η values and that (b) for all η values, the mean thrusts issued from unsteady computation are very similar to those computed with the standard steady approach based on the mean wind.

5. Discussion and conclusions

The main goal of this study was to characterize the influence of the unsteadiness and inhomogeneity of realistic winds on the performance of wind propulsion systems, using a rigid wingsail as a testbed.

Probably the main novelty of this study resides in the application to wingsails performance analysis of methods routinely used to predict wind turbines performance. It is therefore useful to first summarize and further discuss this approach which has been adopted in order to be able to investigate winds with realistic turbulence, which evolve on spatial scales much larger than those typical of the wingsail boundary layers. In this approach, the atmospheric surface or boundary layer flow is resolved in an extended field providing a realistic wind by means of large-eddy simulations. Turbine blades (or the wingsail in our case) geometry and their associated boundary layers are not resolved in the numerical simulation but replaced with blade elements and an aerodynamic force model acting on each element coupled to an unsteady vortex-wake advection model providing the unsteady wake-induced velocity. Two aerodynamic force models have been used. The first is the Beddoes–Leishman model which takes into full account the time delays in the aerodynamic force generation when exposed to temporal variations of the effective wind on each profile. The second is the quasi-steady model where the aerodynamic force depends only on the instantaneous velocity but still includes the unsteadiness of the wind and of the wake. Results have also been obtained with the standard steady approach based on computations performed with the mean wind profiles. In all simulations the unsteadiness and inhomogeneity of the wake has been taken into full account by explicitly solving its free vortical motion. An advantage of this approach, that we plan to use in future

studies, is that it can be easily extended to study additional effects, such as the interaction between multiple wingsails, the analogue of a wind farm in wind energy applications, the interaction with hull-induced parasitic flows or the influence of unsteady wave- or wind-induced ship motions. We believe this to be a significant evolution from standard steady mean wind and/or vortex line approaches which are currently used in unsteady velocity prediction programs or to investigate ships whose propulsion is assisted by multiple wingsails. The use of higher fidelity models, such as those based on large eddy simulations where the wingsail forces are included in the computations with the actuator line approach, are planned in future research.

The effects of wind unsteadiness, shear and inhomogeneity on the wingsail performance have been investigated in a realistic neutral atmospheric surface layer wind. The analyses have been performed on 16 min (1000 s) wind time series, therefore excluding larger time scales where the action of reactive wingsail trim should be included in the analysis. The main findings can be summarized as follows (for the sake of brevity we refer to the aerodynamic driving force as to "thrust"):

- All the considered aerodynamic models (fully unsteady, quasi-steady and steady) predict similar values of the mean thrust. The steady formulation slightly overestimates the thrust but its peak values differ by less than 4% and 7% from fully unsteady and the quasi-steady formulation results respectively.
- Except for the light winds case $\eta = 2$, where the mean true wind velocity is half of the ship velocity, standard deviations of thrust fluctuations are larger than 15% to 20% of the mean thrust. Larger relative fluctuations are observed when $\gamma \gtrsim 90°$ for $\eta = 0.5$ and $\eta = 1$, where the mean apparent wind velocity becomes small. Thrust fluctuations peak values are twice to threefold their standard deviation values.
- The quasi-steady formulation slightly underpredicts thrust fluctuations with respect to the fully unsteady formulation with differences, however, smaller than 10% and 5% in absolute and relative value respectively.
- The mean and fluctuating thrust computed on the optimally twisted wingsail and those computed on the untwisted one differ by less than a few percents for the considered cases where the wingsails are trimmed for maximum thrust.

While we believe that the qualitative nature of these results is general, we expect quantitative predictions to depend on the specific details of the considered configuration. For instance, we have considered a neutral atmospheric surface layer but we show that unsteady effects depend significantly on the features of the incoming wind turbulence. As these features depend on the thermal stratification and on the nature of sea waves, especially in windy configurations, it is likely that results will change if these parameters are changed. It is also important to stress that the results of the present study only apply to rigid wingsails whose dynamic deformation is negligible and in cases where the ship motions are also negligible and in the absence of coherent large-scale parasitic flows induced by the ship hull or superstructures. In situations where these assumptions are not met, depending on the dominant reduced frequencies in the apparent wind, the differences between the results obtained with unsteady, quasi-steady and steady approaches might be much higher than those found in the considered canonical atmospheric surface layer wind. Additional research is, of course, necessary to investigate these situations.

In what concerns the wingsail itself, the presented results depend on the post-stall behavior of the wingsail profile, which is quite smooth for the one-element airfoil we considered but is expected to be much more abrupt when high-lift devices are used, as in most commercial wingsails. Quantitative results, such as the amplitude of the aerodynamic force fluctuations or the mean thrust performance loss are therefore likely to be quite sensitive to the specific wingsail design. For this reason it will be important to extend this study to different types of wingsails and to assess the accuracy of the results with respect to higher fidelity numerical models and to experimental data.

CRediT authorship contribution statement

Clément Bouhourd: Writing – review & editing, Writing – original draft, Visualization, Validation, Software, Methodology, Investigation, Formal analysis, Data curation, Conceptualization. **Laurent Perret:** Writing – review & editing, Supervision, Software, Resources, Project administration, Methodology, Investigation, Funding acquisition, Formal analysis, Conceptualization. **Carlo Cossu:** Writing – review & editing, Writing – original draft, Visualization, Validation, Supervision, Software, Resources, Project administration, Methodology, Investigation, Funding acquisition, Formal analysis, Data curation, Conceptualization.

Declaration of competing interest

The authors declare that they have no known competing financial interests or personal relationships that could have appeared to influence the work reported in this paper.

Acknowledgments

The authors gratefully acknowledge financial support of the French Public Investment Bank through the Mervent 2025 project allocated to Centrale Nantes, France, the use of the Simulator for On/Offshore Wind Farm Applications (SOWFA) developed at NREL (Churchfield et al., 2012) based on the OpenFOAM finite volume framework (Jasak, 2009; OpenCFD, 2011), the use of OpenFAST software, also developed at NREL and an anonymous referee for comments leading to a substantial improvement of the manuscript.

Appendix. Methods

Numerical simulations have been used to compute realistic turbulent winds and to model the unsteady forces acting on the wingsail and the unsteady vortical wake developing downstream.

Large eddy simulations. The wind in the neutral atmospheric surface layer is computed by means of large-eddy simulations performed with the Simulator for On/Offshore Wind Farm Applications (SOWFA) which has been developed for wind energy applications by the US National Renewable Energy Laboratory (NREL) and used by our group in a number of previous wind-energy related studies (Cossu, 2021b,a,c). All details of the formulation, implementation steps and validation of SOWFA are detailed by Churchfield et al. (2010, 2012) so that we here summarize only the main features relevant to the present computations. The filtered incompressible Navier–Stokes equations (see e.g. Deardorff, 1970; Pope, 2000) are solved for the filtered "large-eddy" velocity, pressure and potential temperature fields $\overline{u}_i$, $\overline{p}$, $\overline{\theta}$:

$$\frac{\partial \overline{u}_i}{\partial t} = -\frac{\partial \overline{u}_i \overline{u}_j}{\partial x_j} - \frac{\partial \overline{q}}{\partial x_i} - \frac{\partial \overline{\tau}^r_{ij}}{\partial x_j} + g\delta_{iz}\left(\frac{\overline{\theta} - \theta_0}{\theta_0}\right) - 2\epsilon_{izk}\Omega_z \overline{u}_k,$$

where $\overline{\tau}^r_{ij} = \overline{\tau}^R_{ij} - \overline{\tau}^R_{kk}\,\delta_{ij}/3$, $\overline{\tau}^R_{ij} = \overline{u_i u_j} - \overline{u}_i\overline{u}_j$, $\overline{q} = \overline{p} + \overline{\tau}^R_{kk}/3$ and $\mathbf{\Omega}$ is Earth's rotation rate. The equations are completed by the continuity equation $\partial \overline{u}_i/\partial x_i = 0$. As in this study we only consider the case of a neutral atmospheric boundary layer and we compute winds in the atmospheric surface layer where the effects of the Coriolis acceleration are negligible, the last two terms (buoyancy term and Coriolis acceleration term) in the filtered Navier–Stokes equations are neglected. The anisotropic part of the subgrid stress tensor is modeled by means of an eddy viscosity ν_t as $\overline{\tau}^r_{ij} = -2\nu_t \overline{S}_{ij}$, where $\overline{S}_{ij}$ is the rate of strain tensor associated with the filtered velocity field and the Smagorinsky (1963) model is used $\nu_t = (C_s\overline{\Delta})^2(2\overline{S}_{ij}\overline{S}_{ij})^{1/2}$ with C_s the Smagorinsky constant and $\Delta = (\Delta x \Delta y \Delta z)^{1/3}$, where Δx, Δy and Δz are the cell lengths in the streamwise, spanwise and vertical directions respectively. Periodic boundary conditions are enforced in the horizontal plane with L_x-L_y streamwise-spanwise periodicity. The horizontal extension of the

domain is 200 m × 200 m in this study. Results have been obtained with spatial resolutions of $\Delta x = 2$ m, $\Delta y = 1.5$ m and $\Delta z \approx 1$ m for $z < 50$ m, increasing to $\Delta z \approx 2$ m for $z \to H$. It is assumed that the flow adheres to the Monin and Obukhov (1954) similarity near the ground by implementing (Schumann, 1975) stress boundary conditions at the first cell near the ground which assumed that the filtered vertical velocity profile is logarithmic with the prescribed roughness length z_0. Slip boundary conditions are enforced at the top plane $z = H$ of the solution domain ($H = 300$ m in this study). The filtered equations are discretized in space by means of the finite volume approach implemented in OpenFOAM, a widely used open-source code on top of which SOWFA is built (see Jasak, 2009; OpenCFD, 2011, for more details). A Crank-Nicholson scheme is used to advance in time the discretized equations using the PIMPLE pressure-splitting iterative solution procedure based on the combination of the PISO (Pressure Implicit with Splitting of Operators, Issa, 1986) and the SIMPLE (Semi-Implicit Method for Pressure Linked Equations Caretto et al., 1973) algorithms. A fixed time step $\Delta t = 0.1$ s has been used in the simulations. The filtering and discretization of the equations result in negligible contributions of frequencies larger than approximately 1 Hz to the spectral content of the (resolved) streamwise velocity component at $z_{ref} = 30$ m. Once a fully developed statistically stationary regime is attained in the simulation (after ≈2000 s), the temporal evolution of the velocity field (the wind) in a cross-flow y-z plane is stored for 1000 s with data sampled every 0.1s to be used as inflow boundary condition for the calculation of aerodynamic forces on the wingsail.

Aerodynamic models. Aerodynamic forces acting on the wingsail are computed with OpenFAST, the standard open source tool developed by NREL and widely used to predict and analyze the performance of wind turbines. Here we summarize only the main features relevant to the present computations and refer the reader to the OpenFAST website https://openfast.readthedocs.io where the details of the formulation, implementation steps and validation of OpenFAST are detailed. Aerodynamic forces are computed by means of a blade-element formulation where the wingsail is decomposed into N_z elements ($N_z = 50$ in our computations) on which the aerodynamic force (composed by lift and drag) is computed at the local control point by using the local effective velocity which is the vector sum of the local apparent wind velocity and the velocity induced by the vorticity of the free wake and the (lifting) wing. The latter velocity is computed with a discretized and optimized version of Biot–Savart law. As the wingsail is assumed rigid, the velocity associated to structural oscillations is set to zero. In the quasi-steady approximation, the local aerodynamic tabulated data $C_L(\alpha)$, $C_D(\alpha)$ are used to compute the local elementary aerodynamic force contributions which are then summed to provide the total aerodynamic force. In the fully unsteady formulation, the Beddoes–Leishman model is used to compute the local aerodynamic force. This is a quite complex model introduced by Leishman and Beddoes (1989) (see also Leishman, 2006) to describe the time delays in the force generation that are observed when the unsteady flow is attached, the trailing edge flow separation and the time delays and lift and drag hysteresis associated to dynamic stall. All these effects depend not only on the instantaneous value of the angle of attack and the module of the effective velocity but also on their temporal histories and, as such, are sensitive to the reduced frequency content of the effective velocity. We refer the reader to Damiani and Hayman (2019) for a complete description of the different versions of the Beddoes–Leishman model implemented in OpenFAST, among which the four states formulation of Hansen et al. (2004), Branlard et al. (2022) that we have used.

Free vortex wake. Because of the high unsteadiness and spatial inhomogeneity of the considered apparent winds, no model is used for wake-induced unsteady effects but the vortical wake motion is solved by means of the OLAF free vortex wake module of OpenFAST. The formulation and implementation details of OLAF are described by Shaler et al. (2020), to which we refer the reader for additional information. The vorticity shed in the wake is generated at each time step by the (generally time-varying and spanwise inhomogeneous) lift distribution on the wingsail and then transported and diffused in the freely moving wake. The wake is discretized into $N_{panels} = 20\,000$ elements ($N_z = 50$ new panels along the wing span are emitted at each time step and followed downstream for 400 time steps) whose position and circulation are updated every $\Delta t = 0.1$ s. Each element of the wake is advected using the user-provided velocity field complemented by the wing and wake vorticity-induced velocities. To reduce the computational cost, the self-induced wake deformation is neglected for elements of the wake which are located approximately more than 50 m (one mast height) downstream of the wingsail (the so-called frozen part of the wake). The wake is truncated farther downstream, roughly at 400 m (eight mast heights) where buffer elements replace the action of the truncated part of the wake. Present results were checked to be not sensitive to the wake truncation distance nor to the frozen wake assumption by increasing the number of panels and/or repeating some of the computations without any frozen element of the wake.

References

Bak, C., Zahle, F., Bitsche, R., Kim, T., Yde, A., Henriksen, L.C., Natarajan, A., Hansen, M., 2013. Description of the DTU 10 MW reference wind turbine. In: DTU Wind Energy Report I-0092. DTU Wind Energy. Roskilde (Denmark).

Blevins, R.D., 1990. Flow-Induced Vibration, second ed. Van Nostrand Reinhold, New-York.

Branlard, E., Jonkman, B., Pirrung, G.R., Dixon, K., Jonkman, J., 2022. Dynamic inflow and unsteady aerodynamics models for modal and stability analyses in OpenFAST. J. Phys.: Conf. Ser. 2265, 032044. http://dx.doi.org/10.1088/1742-6596/2265/3/032044.

Caretto, L.S., Gosman, A.D., Patankar, S.V., Spalding, D.B., 1973. Two calculation procedures for steady, three-dimensional flows with recirculation. In: Proceedings of the Third International Conference on Numerical Methods in Fluid Mechanics: II Problems of Fluid Mechanics. Springer, pp. 60–68. http://dx.doi.org/10.1007/BFb0112677.

Chen, Z., Tse, K., Kwok, K., Kim, B., Kareem, A., 2020. Modelling unsteady self-excited wind force on slender prisms in a turbulent flow. Engin. Struct. 202, 109855. http://dx.doi.org/10.1016/j.engstruct.2019.109855.

Churchfield, M.J., Lee, S., Michalakes, J., Moriarty, P.J., 2012. A numerical study of the effects of atmospheric and wake turbulence on wind turbine dynamics. J. Turbul. 13 (N14), http://dx.doi.org/10.1080/14685248.2012.668191.

Churchfield, M.J., Vijayakumar, G., Brasseur, J.G., Moriarty, P.J., 2010. Wind energy-related atmospheric boundary layer large-eddy simulation using OpenFOAM. In: Conference Paper NREL/CP-500-48905. National Renewable Energy Laboratory (NREL). Presented At 19th Symposium on Boundary Layers and Turbulence Keystone, Colorado, August 2-6, 2010.

Cossu, C., 2021a. Evaluation of tilt control for wind-turbine arrays in the atmospheric boundary layer. Wind Energ. Sci. 6, 663–675. http://dx.doi.org/10.5194/wes-6-663-2021.

Cossu, C., 2021b. Replacing wakes with streaks in wind turbine arrays. Wind Energy 24, 345–356. http://dx.doi.org/10.1002/we.2577.

Cossu, C., 2021c. Wake redirection at higher axial induction. Wind Energy Sci 6, 377–388. http://dx.doi.org/10.5194/wes-6-377-2021.

Damiani, R.R., Hayman, G., 2019. The Unsteady Aerodynamics Module for FAST8. Technical Report NREL/TP–(1576) 5000-66347488, National Renewable Energy Laboratory (NREL), http://dx.doi.org/10.2172/1576488.

Deardorff, P.E., 1970. A numerical study of three-dimensional turbulent channel flow at large Reynolds numbers. J. Fluid Mech. 41, 453–480.

DNV-GL, 2019. Environmental conditions and environmental loads. In: Recommended Practice DNVGL-RP-C205. Det Norske Veritas, Norway.

Fossati, F., 2009. Aero-hydrodynamics and the performance of sailing yachts. Adlard Coles Nautical & Politecnico di Milano.

Fuglsang, P., Antoniou, I., Dahl, K.S., Aagaard Madsen, H., 1998. Wind Tunnel Tests of the FFA-W3-241, FFA-W3-301 and NACA 63-430 Airfoils. Technical Report Risoe-R-1041(EN), Forskningscenter Risoe, Denmark.

Hansen, M.H., Gaunaa, M., Madsen, H.A., 2004. A Beddoes-Leishman Type Dynamic Stall Model in State-Space and Indicial Formulations. Technical Report Risø-R-1354(EN), RisøNational Laboratory., Roskilde, Denmark.

Issa, R.I., 1986. Solution of the implicitly discretised fluid flow equations by operator-splitting. J. Comput. Phys. 62, 40–65.

Jasak, H., 2009. OpenFOAM: open source CFD in research and industry. Int. J. Naval Arch.Oc. Eng 1, 89–94.

Laursen, R., Patel, H., Sofiadi, D., Zhu, R., Nelissen, D., Van Seters, D., Pang, E., 2023. Potential of Wind-Assisted Propulsion for Shipping. Technical Report, European Maritime Safety Agency (EMSA), Lisbon.

Leishman, G., 2006. Principles of Helicopter Aerodynamics with CD Extra. Cambridge University Press.

Leishman, J., Beddoes, T., 1989. A semi-empirical model for dynamic stall. J. Amer. Helicopter Soc 34, 3–17.

Marchaj, C.A., 1996. Aero-Hydrodynamics of Sailing, second ed. Adlard Coles Nautical.

Monin, A., Obukhov, A., 1954. Basic laws of turbulent mixing in the surface layer of the atmosphere. Contrib. Geophys. Inst. Acad. Sci. USSR 151, e187.

OpenCFD, 2011. OpenFOAM - ThE Open Source CFD Toolbox – User's Guide, 2.4 ed. OpenCFD Ltd. UK, URL http://www.openfoam.org.

Pope, S.B., 2000. Turbulent Flows. Cambridge U. Press, Cambridge, UK.

Schumann, U., 1975. Subgrid scale model for finite difference simulations of turbulent flows in plane channels and annuli. J. Comput. Phys. 18, 376–404. http://dx.doi.org/10.1016/0021-9991(75)90093-5.

Shaler, K., Anderson, B., Martínez-Tossas, L.A., Branlard, E., Johnson, N., 2023. Comparison of free vortex wake and blade element momentum results against large-eddy simulation results for highly flexible turbines under challenging inflow conditions. Wind Energy Sci. 8, 383–399. http://dx.doi.org/10.5194/wes-8-383-2023.

Shaler, K., Branlard, E., Platt, A., 2020. OLAF User's Guide and Theory Manual. Technical Report NREL/TP-5000-75959, National Renewable Energy Lab.(NREL, Golden, CO (United States), http://dx.doi.org/10.2172/1659853.

Smagorinsky, J., 1963. General circulation experiments with the primitive equations: I. the basic experiment. Mon. Weather Rev. 91, 99–164. http://dx.doi.org/10.1175/1520-0493(1963)091<0099:GCEWTP>2.3.CO;2.

Turnock, S., Magherini, M., Campbell, I., 2014. Parameters affecting the performance of the C-class wingsail. Intl. J. of Small Craft Tech 156, 21–34.

Wyngaard, J.C., 2010. Turbulence in the Atmosphere. Cambridge University Press.